Journal of Materials Chemistry A

ROYAL SOCIETY OF CHEMISTRY

PAPER

View Article Online
View Journal | View Issue

Cite this: *J. Mater. Chem. A*, 2020, **8**, 2613

The stability and reaction mechanism of a LiF/electrolyte interface: insight from density functional theory†

Bingkai Zhang,[ab] Zhan Lin, *[a] Haibiao Chen,[b] Lin-Wang Wang*[c] and Feng Pan *[b]

In a Li-metal battery, a solid lithium fluoride (sLiF) film, as a coating layer, is widely used to stabilize both the Li-metal and the liquid electrolyte (LE) to suppress unwanted redox shuttles. The sLiF/LE interface significantly affects the performance of the Li-metal battery. Here, to understand the chemistry and the Li-ion transport properties of the solid–liquid interface, we study interfacial reactions and dynamics at the interface between sLiF and a liquid electrolyte (EC, DMC, and $LiPF_6$) by using a quantum mechanics method. $LiPF_6$ is found to be chemically unstable at the sLiF/LE interface, and a resistive solid–liquid electrolyte interphase (SLEI) for Li-ion transport forms at the interface. The mobility of the electrolyte molecules and Li-ions near the sLiF/LE interface is much lower than that in a bulk liquid electrolyte. Such a molecular-level understanding of the interfacial processes provides the basis to develop a new interface between a solid and a liquid electrolyte for better Li-ion batteries.

Received 15th September 2019
Accepted 21st December 2019

DOI: 10.1039/c9ta10170e

rsc.li/materials-a

Introduction

The next-generation high energy density lithium-ion batteries (LIBs), such as Li/S_8 (ref. 1–3) and Li/O_2 (ref. 4 and 5) batteries, rely on Li-metal as the anode and a liquid electrolyte (LE) as the ion-conducting phase. A liquid electrolyte provides a high ionic conductivity and can easily wet and fill porous electrodes, resulting in a large interface between the electrode and the storage phase. However, the solid electrolyte interphase (SEI) formed from the Li-metal and LE is usually beyond control and easy to break during battery cycling.[6–9] In order to control and optimize the interface behavior, a sLiF film, as an artificial interphase, is widely used.[10–15] sLiF is also suggested to improve the surface diffusion of ions and therefore it facilitates smooth deposition and dissolution on the surface of Li metal.[16,17]

Chemically speaking, the solid–liquid interphase comes from the sacrificial decomposition of the electrolyte components, *e.g.*, through the single-electron reduction of organic molecules. In a sLiF coating layer, although crystalline LiF is a key component, other phases including nonstoichiometric or amorphous LiF or grain boundaries can significantly affect Li-ion transport. A coating layer consisting of crystalline LiF alone will certainly fail to function because crystalline LiF is an insulator not only to electrons but also to ions. Recent observations argued that an artificial solid–liquid interface, *i.e.*, sLiF/LE, increases the total resistance of lithium batteries.[4,18,19]

However, to the best of our knowledge, there is a lack of theoretical investigations on such a sLiF/LE interface. It is interesting to know whether the side-reaction of electrolytes occurs on sLiF and to know how Li-ion migrates at the sLiF/LE interface. Here, we attempted to study the sLiF/LE interface by *ab initio* molecular dynamics (AIMD) based on the quantum mechanics (QM) simulation technique. These modeling techniques are well suited to the investigation of such properties and have been applied successfully to a variety of studies on ionic conductors[20–22] and interfaces.[23]

Results and discussion

Structural modeling

The most classical liquid electrolyte is perhaps the "$LiPF_6$–EC–DMC" solution, where EC is ethylene carbonate, DMC is dimethyl carbonate, and the concentration of $LiPF_6$ is 1 mol L^{-1} in EC/DMC (1/1 vol%). Fig. 1a shows the $LiPF_6$–EC–DMC system built using a 3D amorphous cell with periodic boundary conditions, in which Li^+ and PF_6^- ions were initially associated. After the AIMD simulations, the representative snapshot of the solution structure in Fig. 1b shows that a solvated Li is bonded to the oxygen atoms from three EC or DMC molecules and one PF_6^-. From the AIMD simulations, the pair correlation functions between Li and oxygen atoms from EC/DMC are shown in Fig. 1c. The first peak of the Li–O pair correlation function (PCF) is at approximately 1.9 Å with a coordination number of ~2.6. The first peak of the Li–F

[a]*School of Chemical Engineering and Light Industry, Guangdong University of Technology, Guangzhou 510006, China. E-mail: zhanlin@gdut.edu.cn*

[b]*School of Advanced Materials, Peking University, Shenzhen, China. E-mail: panfeng@pkusz.edu.cn*

[c]*Materials Sciences Division, Lawrence Berkeley National Laboratory, Berkeley, CA 94720, USA. E-mail: lwwang@lbl.gov*

† Electronic supplementary information (ESI) available. See DOI: 10.1039/c9ta10170e

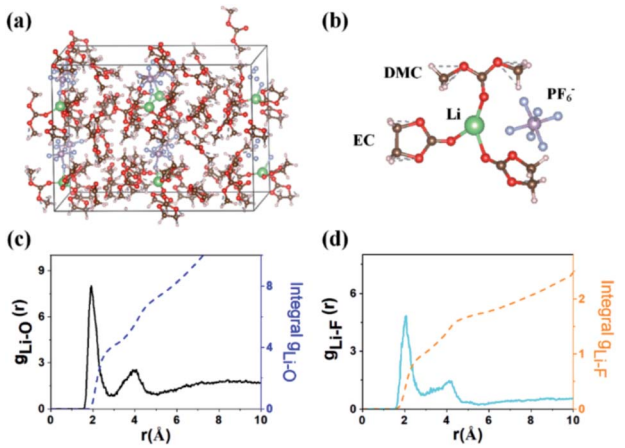

Fig. 1 (a) Side view of a schematic representation of liquid electrolytes. (b) Representative local structure of the coordination environments around a Li-ion. (c) Li–O and (d) Li–F pair correlation functions (solid lines) and their integrals (dashed lines) for LEs (a) from a 60 ps NVT AIMD simulation at 800 K.

PCF is at approximately 2.0 Å with a coordination number of ~0.8 (Fig. 1d). In addition, we did another AIMD simulation where Li^+ and PF_6^- ions were initially dissociated (the distance between Li and P is about 6 Å). Nearly a quarter of $LiPF_6$ molecules are kept up their dissociated state after a 60 ps NVT simulation. The Li–P distance *versus* simulation time is shown in Fig. S1.† Therefore, we suggest $LiPF_6$ remains in the ion-paired state (*i.e.*, the representative structure in Fig. 1b) in liquid electrolytes.

The de-solvation of solvated Li-ions and PF_6^- dissociation on the sLiF surface

First, we need to evaluate the de-solvation process to determine the last species that remain with the Li-ion before complete de-solvation. The partial de-solvation process significantly depends on the competitive interaction of solvents and PF_6^- with Li-ions, as quantified by the solvation energies shown in Fig. 2. As defined by eqn (1), the large negative values of solvation energy mean that there are strong interactions between Li-ions and solvents or PF_6^-. For EC and DMC, the entire solvation number ranges from 1 to 4, and their solvation energies are always smaller than that of PF_6^- in an attempt to remain in the primary Li-ion solvation sheath. These results show that PF_6^- is the last to be desolvated or even co-intercalated into the diffusion channel.

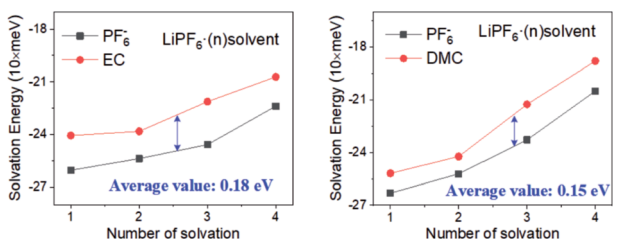

Fig. 2 Solvation energy of solvent molecules in $LiPF_6$·EC- and $LiPF_6$·DMC-based electrolytes.

Therefore, a question is raised regarding whether PF_6^- undergoes reductive decomposition on the sLiF(100) surface and whether it affects the reductive activity of the carbonate molecules. For this, we calculated the single electron reduction of isolated organic electrolytes and anion and electron affinity energies (Fig. S2 and S3 in ESI†). As defined by eqn (2), the more negative value of electron affinity energy is, the higher reductive activity the configuration will have. For isolated molecules, the decomposition of PF_6^- is found to be slower than those of both EC and DMC; hence it is thermodynamically improbable for an isolated PF_6^- to gain an electron. The only possibility for PF_6^- to gain an electron is to associate with a Li-ion. Fig. S4 and S5 in the ESI† show the optimized structures of Li·(*n*)solvents before and after single-electron reduction. The electron affinity energy of solvents in Fig. S5† shows that the existence of Li-ions increases the reductive activity of the solvents. The effect of Li-ions on the reductive activity of the solvents and PF_6^- suggests that solvent molecules or PF_6^- coordinated with Li-ions may experience an electrochemical reaction by accepting an electron.

To prove this point, Fig. 3 presents the optimized structure of the Li-ion solvation complex containing PF_6^- after single-electron reduction. For the contact ion pair solvation, the reductive reaction is more complicated, because the electron can be distributed on either the solvent or PF_6^-. Electron attack on PF_6^- directly leads to the breakage of the P–F bond, and most importantly, it generates molecular LiF units. Fig. 4 shows the calculated electron affinity energies of the corresponding solvation complexes. Unexpectedly, the received electron prefers to reside on PF_6^- instead of a solvent molecule, and PF_6^- has a dramatically higher electron affinity energy than solvents. Overall, in LE, PF_6^- tends to experience electrochemical reactions at the sLiF/LE interface.

Reactive dynamics and Li-ion diffusion study at the sLiF/LE interface

To gain a clearer insight into the reaction dynamics and Li-ion mobility at the sLiF/LE interface, we utilized the AIMD for computing the dynamics of the sLiF/LE interface. We studied the stability of the sLiF/LE interface with a five-layer LiF(100)

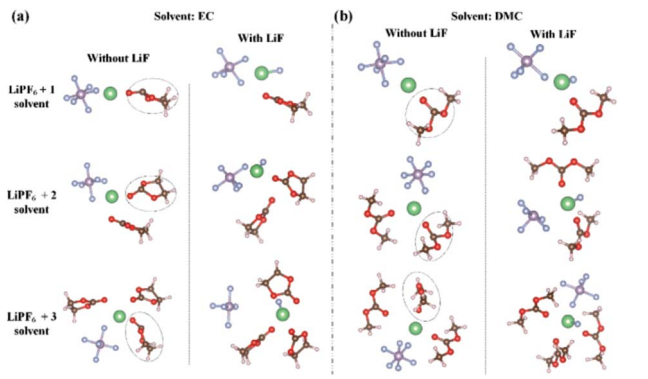

Fig. 3 Optimized structures of ($LiPF_6$·(*n*)solvent) solvation complexes after single-electron reduction with and without LiF formation. The reduced solvent is highlighted with dotted circles.

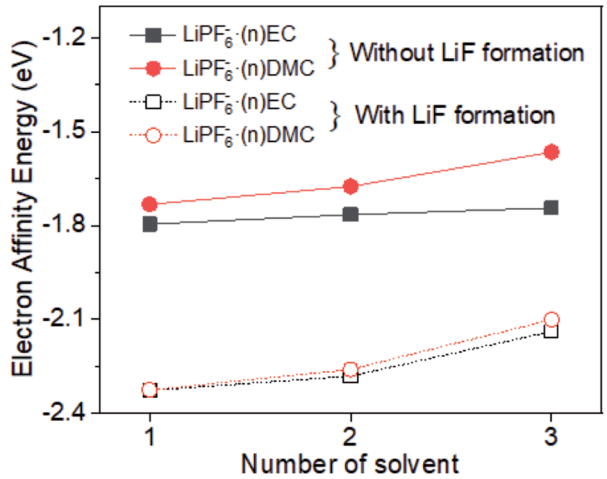

Fig. 4 Calculated electron affinity energy of ($LiPF_6$·(*n*)solvents) solvation sheaths.

surface using a 30 ps AIMD simulation at 800 K. The purpose of the temperature is to accelerate possible reactions or migration to a time scale suitable for AIMD. It is important to note that the AIMD studies on the electrochemical interface lack electrochemical driving force in the simulation method. In reality, the reaction would occur at ambient temperature due to the applied potential.

After a 30 ps AIMD simulation, two stoichiometric (a and b) and two Li-excess (c and d) sLiF/LE interfaces are shown in Fig. 5. The two stoichiometric interfaces suggest their geometric structures do not change too much with the simulation time. There is no O–C or H–C bond-breaking for EC or DMC molecules during the simulation. However, in Li-excess configurations (one additional Li at the sLiF/LE interface), as shown in Fig. 5c and d, electrolytes near the interface precede dissociation or binding interaction. More importantly, in the first Li-excess configuration (setting additional Li close to $LiPF_6$), structural optimization

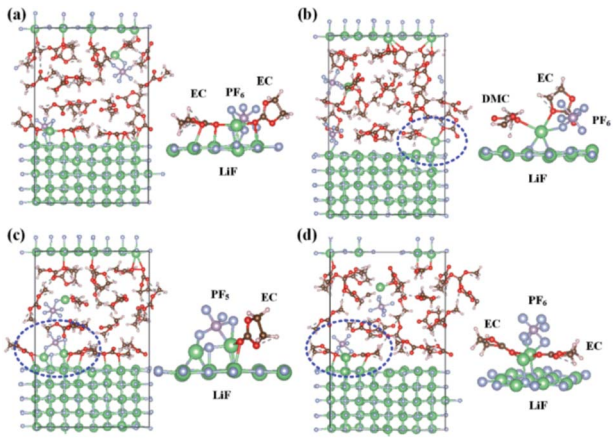

Fig. 5 (a and b) Two stoichiometric sLiF/LE interfacial structures after a 30 ps NVT AIMD simulation (800 K). (c and d) Two Li-excess structures of the sLiF/LE interface after a 30 ps NVT AIMD simulation (800 K). The coordination environments around a Li-ion highlighted by dashed circles.

leads to quick decomposition of PF_6^- with the aid of the additional Li, which is consistent with the result of AIMD. Because this decomposition reaction occurs during optimization, it is supposed to have a very low energy barrier. For another Li-excess configuration (setting additional Li close to $LiPF_6$ and EC), molecular LiO units come into being on the sLiF surface after relaxation and the oxygen atoms come from EC molecules. Thus, decomposition reactions might be activated with the aid of the Li-excess configuration. In Fig. 5c and d, the AIMD simulation also suggests that once electrolytes bind with the LiF surface and LiF/LiO units formed on the LiF surface, their location variations become little, passivating them against further migration. A previous study by Jiang and co-authors reported a similar AIMD study on an anode-electrolyte interface for several electrolytes.[24] They showed that an electrolyte near the interface precedes reduction and this reduction reaction depends strongly on the surface functionalization (requiring specific alignments and proximity) and the presence of $LiPF_6$ salt. In addition, they also showed the decomposition of PF_6^- into LiF with the aid of oxygen/hydroxyl termination, and propylene carbonate (PC) molecules decompose quickly in the presence of Li. Their results suggest solid-electrolyte interphase formation at the graphite/electrolyte interface, which is consistent with our results on the LiF(100) surface.

For Li-ion and PF_6^- mobility analysis, in Fig. 6 we show the mean square displacement (MSD) of Li and PF_6^- (by tracking the P atom) for bulk LE and the sLiF/LE interface. These plots in Fig. 6 reveal three main features. First, in bulk LE, PF_6^- diffuses faster than Li even though it is the heavier species. This can be attributed to the fact that solvent molecules interact more strongly with Li than with PF_6^-. Second, for Li and PF_6^- near the sLiF surface, Li diffuses faster than PF_6^- because of the stronger interaction between PF_6^- and sLiF and the steric effects of the sLiF surface. Two F atoms are located at the top Li site of sLiF and the Li atom is at the bridge site of sLiF. The structure of PF_6·Li matches well with that of the sLiF(100) lattice. Third, for Li and PF_6^- away from the sLiF surface, Li and PF_6^- have high diffusivities than those near the sLiF surface but are still below those in LE. The structural fluctuation of the first solvation shell is strongly correlated with adjacent molecules. In this respect, we suggest that the mobility of PF_6^- and Li-ions can be related to the low mobility of the

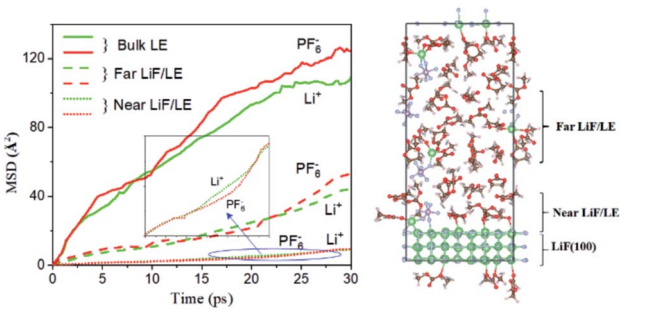

Fig. 6 Mean square displacement plots of Li-ions and PF_6^- obtained from 30 ps NVT at 800 K simulations in bulk LE and the sLiF/LE interface. The inset shows the MSD of Li-ions and PF_6^- near the LiF/LE interface.

electrolyte molecules near the sLiF surface. In addition, in Fig. S6,† the Li-ion trajectory density over the AIMD simulated time scale enables the migration maps to be visualized.[25,26] This figure shows that the diffusion region in LE (Fig. S6a in ESI†) is obviously larger than that in the sLiF/LE interface (Fig. S6b–S6d in ESI†), indicating a higher Li-ion mobility.

To further prove the low mobility of LE molecules on the sLiF/LE interface, the site displacement function (SDF) of EC and DMC as a function of simulation time by tracking the C atom is introduced, as shown in Fig. S7.† The SDF equation is defined as $d(t) = |r(t) - r(0)|$, *i.e.*, the distance between the position of the C atom at time t ($r(t)$) and the initial position of the C atom at time (0). A larger SDF value means a larger diffusion distance. The SDF values of solvent molecules in LE (solid lines) are larger than those in sLiF/LE (dashed lines), therefore, solvent molecules can migrate further away from the initial sites. In addition, EC molecules are more mobile than DMC in both systems. Overall, the mobilities of EC and DMC are strongly limited in the sLiF/LE system. The low mobility of solvent molecules in the sLiF/LE system may lead to the formation of a resistive solid–liquid electrolyte interphase.

Conclusions

In summary, we used QM-based DFT and AIMD to evaluate the interfacial dynamics of sLiF/LE and successfully explain the Li-ion mobility at the interface. The solvation energy suggests that during the de-solvation process the energy for removing an EC or DMC molecule is less than that for PF_6^-, indicating that PF_6^- will remain in the solvation shell and participate in subsequent reduction decomposition. The Li-ion leads to the instability of PF_6^-, indicating that if there is no PF_6^- existing in the Li-ion solvent structure, the LiF interphase cannot be formed. The AIMD calculations suggest that there is an initial decomposition reaction of PF_6^-, and stable $PF_6 \cdot Li$ or $2Li \cdot 2O$ species are adsorbed on the sLiF surface due to symmetry match, which can be in better contact with both the Li (bonding with F sites of sLiF) and the F (bonding with Li sites of sLiF) in LE. The decomposition reaction of $LiPF_6$ occurs with the aid of Li in LE or defect of the sLiF surface. Low Li-ion mobility arises from the steric effect of sLiF and the interaction between the electrolytes and sLiF, which leads to low mobility of solvent molecules and a rather high energy barrier.

We assume that the low Li-ion conductivity interphase may form at other interfaces between sLiF and liquid electrolytes. Further analytical and experimental work is required to obtain more insight into the chemical identity and the formation mechanism of the resistive solid–liquid electrolyte interphase.

Methods

QM-based density functional theory (DFT) simulations with van der Waals interaction were performed by using the projector augmented wave (PAW)[27] Vienna *ab initio* simulation package (VASP)[28] for energy minimization calculations and AIMD for reactive dynamics and Li-ion diffusion. The exchange and correlation energies were calculated using the Perdew, Burke, and Ernzerhof (PBE) functions within the generalized gradient approximation (GGA).[29] All calculations were carried out with spin polarization with a plane-wave cutoff energy of 400 eV. The energy minimization criterion is <0.02 eV $Å^{-1}$ for all forces on free atoms. Grimme's DFT-D3 method (dispersion corrections for DFT functionals) was used.[30] QM-based AIMD simulation was used to evaluate the diffusion and reactive dynamics under the NVT ensemble. Only the gamma point of the Brillouin zone with no consideration of symmetry is sampled in the AIMD computations.

Here, the stable (100) face of sLiF with alternating Li^+ and F^- ions on adjacent lattice positions is considered in this work. The sLiF (100) surface has been suggested by transmission electron microscopy (TEM) imaging[31–33] and experiment.[16] Two $p(4 \times 8)$ surface cells of LiF(100) were modelled: three-layer and five-layer. For the two slabs, vacuum spacings of 32 Å and 17 Å were used to separate the image interactions between the slabs, respectively. The three-layer LiF(100) is used to model the large sLiF/LE interface, and the middle layer is fixed during AIMD simulations. The sLiF/LE interface is modelled by packing the EC, DMC and $LiPF_6$ in the LiF(100) box. In the packing process, their molar ratio is about 6.1 : 5.8 : 1.

The initial configuration is set up using the 3D amorphous cell with periodic boundary conditions (16 × 24 × 18 Å) at an initial concentration of 1 mol L^{-1} of $LiPF_6$ in EC/DMC (1/1 vol%). In the amorphous cell module simulation, the force field of the CVFF potential from the Materials Studio code was adopted.[34] To ensure the system from AIMD is equilibrated and reliable, we firstly adopt the NPT (T = 450 K and P = 0 bar) ensemble in the simulations for 10 ps. Then, the system was cooled to T = 400 K at a rate of 5 K ns^{-1}. At 400 K, the system is relaxed for 10 ps and the equilibrium value of the volume is obtained. Secondly, the system was simulated in the NVT (T = 400 K) ensemble for 60 ps to make sure that the systems reached the equilibrium states. A Nose–Hoover thermostat was employed for the NVT AIMD simulations.[35,36] Last, we compared the diffusion coefficients of Li^+ and PF_6^- in EC/DMC electrolytes using both the mean square displacement (MSD) and velocity autocorrelation function (VACF) methods. The calculated diffusion coefficient based on MSD and VACF is about 3.2×10^{-10} and 8.3×10^{-10} cm^2 s^{-1} at a temperature of 400 K, respectively. These values were of the same order of magnitude as those calculated using the classical molecular dynamics.[37] In addition, the applied potential is an important electrochemical driving force for interfacial reactions. For future studies, it may be of interest to use a constant potential method to investigate the effects of applied potential on interfacial reactions.[38]

The solvation energy and electron affinity energy were calculated using the solvation model for the plane wave DFT code VASP. To evaluate the role of the environment, the implicit solvation model was used to simulate the solvent effect in the calculations. Grimme's DFT-D3 method was used.[30] The gamma k-point set was used for lattice optimizations. The dielectric constants for EC, DMC, and EC/DMC were set as 90.3, 3.2, and 46.0 and were used to represent the solvents for the solvation model. Here, the dielectric constant of EC/DMC was approximated by averaging the dielectric constants of the two solvents. Solvation energy of the nth solvent is defined as:

$$E_{\text{solvation-energy}} = E_{\text{LiPF}_6\cdot n\cdot\text{solvent}} - E_{\text{LiPF}_6\cdot(n-1)\cdot\text{solvent}} \quad (1)$$

which suggests a giving off energy as the nth solvent interacts with $LiPF_6$. Electron affinity energy of a configuration is defined as:

$$E_{\text{electron-affinity-energy}} = E_{(N+1)} - E_{(N)} \quad (2)$$

where $E_{(N+1)}$ and $E_{(N)}$ are the total ground-state energies in the single charged ($N+1$ number of valence electrons) and neutral (N number of valence electrons) configurations. The more negative value of electron affinity energy is, the higher reductive activity the configuration will have. The equilibrium geometries of $LiPF_6$–EC–DMC configurations were examined in a large cell of $25 \times 25 \times 25$ Å.

Conflicts of interest

There are no conflicts to declare.

Acknowledgements

This work was financially supported by startup R&D funding from the One-Hundred Young Talents Program of the Guangdong University of Technology (No. 22041331901), National Key R&D Program of China (2016YFB0700600), Soft Science Research Project of Guangdong Province (No. 2017B030301013), Shenzhen Science and Technology Research Grant (ZDSYS201707281026184), and National Natural Science Foundation of China (No. 51703070). Wang was supported by the Assistant Secretary for Energy Efficiency and Renewal Energy of the U.S. Department of Energy under the Battery Materials Research (BMR) program.

Notes and references

1 W. Li, G. Zheng, Y. Yang, Z. W. Seh, N. Liu and Y. Cui, *Proc. Natl. Acad. Sci. U. S. A.*, 2013, **110**, 7148–7153.
2 X. Ji, K. T. Lee and L. F. Nazar, *Nat. Mater.*, 2009, **8**, 500.
3 Y.-S. Su and A. Manthiram, *Nat. Commun.*, 2012, **3**, 1166.
4 M. R. Busche, T. Drossel, T. Leichtweiss, D. A. Weber, M. Falk, M. Schneider, M.-L. Reich, H. Sommer, P. Adelhelm and J. Janek, *Nat. Chem.*, 2016, **8**, 426.
5 Z. Peng, S. A. Freunberger, Y. Chen and P. G. Bruce, *Science*, 2012, **337**, 563–566.
6 W. Xu, J. Wang, F. Ding, X. Chen, E. Nasybulin, Y. Zhang and J.-G. Zhang, *Energy Environ. Sci.*, 2014, **7**, 513–537.
7 D. Aurbach, E. Zinigrad, Y. Cohen and H. Teller, *Solid State Ionics*, 2002, **148**, 405–416.
8 B. Zhang, R. Tan, L. Yang, J. Zheng, K. Zhang, S. Mo, Z. Lin and F. Pan, *Energy Storage Mater.*, 2018, **10**, 139–159.
9 D. Lin, Y. Liu and Y. Cui, *Nat. Nanotechnol.*, 2017, **12**, 194.
10 J. Zhao, L. Liao, F. Shi, T. Lei, G. Chen, A. Pei, J. Sun, K. Yan, G. Zhou, J. Xie, C. Liu, Y. Li, Z. Liang, Z. Bao and Y. Cui, *J. Am. Chem. Soc.*, 2017, **139**, 11550–11558.
11 J. Xie, L. Liao, Y. Gong, Y. Li, F. Shi, A. Pei, J. Sun, R. Zhang, B. Kong, R. Subbaraman, J. Christensen and Y. Cui, *Sci. Adv.*, 2017, **3**, eaao3170.
12 Y. Yuan, F. Wu, Y. Bai, Y. Li, G. Chen, Z. Wang and C. Wu, *Energy Storage Mater.*, 2019, **16**, 411–418.
13 Z. Peng, N. Zhao, Z. Zhang, H. Wan, H. Lin, M. Liu, C. Shen, H. He, X. Guo, J.-G. Zhang and D. Wang, *Nano Energy*, 2017, **39**, 662–672.
14 J. Ko and Y. S. Yoon, *Ceram. Int.*, 2019, **45**, 30–49.
15 T. Liu, L. Lin, X. Bi, L. Tian, K. Yang, J. Liu, M. Li, Z. Chen, J. Lu, K. Amine, K. Xu and F. Pan, *Nat. Nanotechnol.*, 2019, **14**, 50–56.
16 L. Fan, H. L. Zhuang, L. Gao, Y. Lu and L. A. Archer, *J. Mater. Chem. A*, 2017, **5**, 3483–3492.
17 S. Choudhury and L. A. Archer, *Adv. Electron. Mater.*, 2016, **2**, 1500246.
18 Y. Yamada, F. Sagane, Y. Iriyama, T. Abe and Z. Ogumi, *J. Phys. Chem. C*, 2009, **113**, 14528–14532.
19 D. Aurbach, *J. Power Sources*, 2000, **89**, 206–218.
20 Y. Mo, S. P. Ong and G. Ceder, *Chem. Mater.*, 2012, **24**, 15–17.
21 Y. Hao, M. S. Bharathi, L. Wang, Y. Liu, H. Chen, S. Nie, X. Wang, H. Chou, C. Tan, B. Fallahazad, H. Ramanarayan, C. W. Magnuson, E. Tutuc, B. I. Yakobson, K. F. McCarty, Y.-W. Zhang, P. Kim, J. Hone, L. Colombo and R. S. Ruoff, *Science*, 2013, **342**, 720–723.
22 S. Shi, P. Lu, Z. Liu, Y. Qi, H. L. Jr, H. Li and S. J. Harris, *J. Am. Chem. Soc.*, 2012, **134**, 15476–15487.
23 T. Cheng, B. V. Merinov, S. Morozov and W. A. Goddard, *ACS Energy Lett.*, 2017, **2**, 1454–1459.
24 P. Ganesh, P. R. C. Kent and D.-e. Jiang, *J. Phys. Chem. C*, 2012, **116**, 24476–24481.
25 Z. Zhu, I.-H. Chu, Z. Deng and S. P. Ong, *Chem. Mater.*, 2015, **27**, 8318–8325.
26 Z. Deng, Z. Zhu, I.-H. Chu and S. P. Ong, *Chem. Mater.*, 2017, **29**, 281–288.
27 P. E. Blöchl, *Phys. Rev. B: Condens. Matter Mater. Phys.*, 1994, **50**, 17953–17979.
28 G. Kresse and J. Furthmüller, *Phys. Rev. B: Condens. Matter Mater. Phys.*, 1996, **54**, 11169–11186.
29 J. P. Perdew, K. Burke and M. Ernzerhof, *Phys. Rev. Lett.*, 1996, **77**, 3865–3868.
30 S. Grimme, J. Antony, S. Ehrlich and H. Krieg, *J. Chem. Phys.*, 2010, **132**, 154104.
31 L. Suo, O. Borodin, T. Gao, M. Olguin, J. Ho, X. Fan, C. Luo, C. Wang and K. Xu, *Science*, 2015, **350**, 938–943.
32 Y. Yang, Z. Wang, R. Zhou, H. Guo and X. Li, *Mater. Lett.*, 2016, **184**, 65–68.
33 Y. Sun, H.-W. Lee, G. Zheng, Z. W. Seh, J. Sun, Y. Li and Y. Cui, *Nano Lett.*, 2016, **16**, 1497–1501.
34 S. Plimpton, *J. Comput. Phys.*, 1995, **117**, 1–19.
35 B. Zhang, Z. Lin, H. Dong, L.-W. Wang and F. Pan, *J. Mater. Chem. A*, 2020, **8**, 342–348.
36 B. Zhang, L. Yang, L.-W. Wang and F. Pan, *Nano Energy*, 2019, **62**, 844–852.
37 C. M. Tenney and R. T. Cygan, *J. Phys. Chem. C*, 2013, **117**, 24673–24684.
38 Z. Wang, Y. Yang, D. L. Olmsted, M. Asta and B. B. Laird, *J. Chem. Phys.*, 2014, **141**, 184102.